Check for updates

ChemPubSoc Europe

DOI: 10.1002/cssc.201902013

CHEMSUSCHEM Full Papers

VIP *Very Important Paper*



In Situ Self-Assembly of Core–Shell Multimetal Prussian Blue Analogues for High-Performance Sodium-Ion Batteries

Jinwen Yin, Yi Shen, Chang Li, Chenyang Fan, Shixiong Sun, Yi Liu, Jian Peng,* Li Qing, and Jiantao Han*[a]

Metal–organic frameworks (MOFs), such as Prussian blue and its analogues (PB and PBAs) with open frameworks have attracted tremendous attentions as cathode materials for sodium-ion batteries, owing to their simple method of synthesis and high theoretical specific capacity. In this study, core–shell-structured PBAs are prepared by an in situ self-assembly method. Owing to the advantages of both constituents, the as-prepared core–shell PBAs show excellent rate and cycling electrochemical properties through a dual-level-controlled charge–discharge depth mechanism. It delivers a specific capacity of 104.3 mAh g^{-1} at 0.1 C, as well as a remarkably enhanced cycle performance, giving 88.3% of its initial capacity over 1000 cycles at 300 mA g^{-1}. In particular, the coating strategy described herein could be extended to other MOF materials, leading to wider application in energy storage.

Introduction

For the past few decades, long-life and low-cost rechargeable batteries have been in high demand for grid-scale electrical energy storage systems (EESs).[1] Thanks to their advantageous energy density and lifespan, lithium-ion batteries (LIBs) are extensively applied in portable devices and electric cars. However, the development of LIBs for EES application faces great risk from limited lithium resources.[2] Therefore, low-cost sodium-ion batteries (SIBs), which share similar chemistry with LIBs but with much higher metal reserves, have attracted much attention for application in EESs as an alternative to LIBs.[3]

Recently, analogues of Prussian blue (PBAs), a three-dimensional metal–organic framework (MOF), can be facilely synthesized from low-cost and nontoxic precursors on a large scale, which have been investigated as promising cathode materials for SIBs in both organic and aqueous electrolyte systems.[4] Usually, the crystal structure of PBAs can be denoted as $\mathbf{A}_x\mathbf{B}[\mathbf{C}(CN)_6]_y\cdot\square_{1-y}\cdot z H_2O$, where **A** represents Na or K and **B** and **C** are transition-metal ions and □ represents a vacancy.[5] The values of *x*, *y*, and *z* depend on the stoichiometry). According to the number of Na^+ stored per formula unit, PBAs could typically be divided into single-electron transfer type (where **B** = Ni, Cu, Zn, Ce, etc.) and dual-electron transfer type (where **B** = Fe, Co or Mn), with theoretical specific capacities of 85 and 170 mAh g^{-1}, respectively.[6] Cui and co-workers reported fabricating three-electron transfer type Mn-based PBAs and achieved an ultrahigh specific capacity of 210 mAh g^{-1}, which constitutes a high-performance candidate and also enlarges the PBA family.[7] However, most PBAs show poor cyclability and low capability as cathode materials for sodium-ion batteries, owing to the abundant vacancies in the lattice, resulting in large lattice distortions during the charge–discharge process.[2c,4d,5a,8] Many methods have been applied to optimize the crystallization process and morphology of PBAs to enhance their electrochemical performance as cathodes for SIBs. For instance, the groups of Yang and Guo reported a low-speed co-precipitation method to synthesize iron-based PBAs with fewer defects, which achieved a highly reversible storage reaction of two sodium ions with a Coulombic efficiency of nearly 100%.[4c,9] Goodenough and co-workers synthesized dehydrated $Na_2MnFe(CN)_6$, which delivered a high capacity with flat charge–discharge plateaus, by removing the interstitial H_2O.[10] In our previous work, we developed a chelating agent–surfactant co-assisted crystallization method to synthesize highly crystallized ternary-metal PBAs. By controlling lattice distortion, the cycling and rate performance were both remarkably improved. Furthermore, we found that nickel hexacyanoferrate (Ni-HCF) could effectively avoid side reactions with the electrolyte and manifest superior rate performance.[5b]

In this work, a highly crystallized core–shell cobalt/nickel hexacyanoferrate coated by Ni-HCF (CoNi-HCF@Ni-HCF) PBA was fabricated by using an in situ self-assembly method (Figure 1). The cycle life and rate performance were successively improved by combining the advantages of both constituents through a new dual-level controlling charge–discharge depth mechanism, which refers to inactive metal doping in pure cobalt hexacyanoferrate[5b] and coated by Ni-HCF to

[a] J. Yin, Y. Shen, C. Li, C. Fan, S. Sun, Y. Liu, J. Peng, Prof. L. Qing, Prof. J. Han
State Key Laboratory of Material Processing and Die & Mould Technology
School of Materials Science and Engineering
Huazhong University of Science and Technology
Wuhan 430074 (P.R. China)
E-mail: pj9301@hust.edu.cn
jthan@hust.edu.cn

Supporting information and the ORCID identification number(s) for the author(s) of this article can be found under: https://doi.org/10.1002/cssc.201902013.

© 2019 Wiley-VCH Verlag GmbH & Co. KGaA, Weinheim

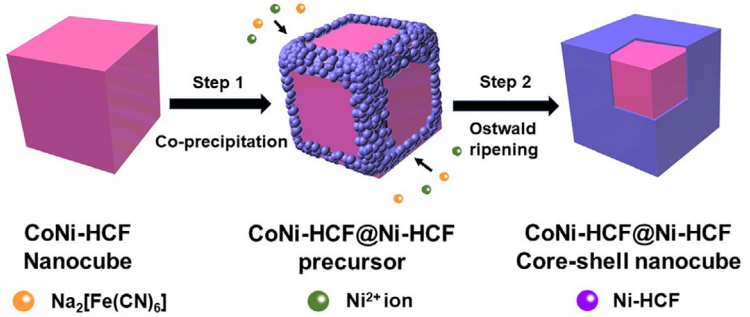


Figure 1. Synthesis procedure of CoNi-HCF@Ni-HCF core–shell nanocubes.

attain a balance among capacity, cycling and rate performance. The results showed that the excessive lattice distortion was suppressed by introducing inactive metal into the core, and Ni-HCF coating suppressed side reactions with the electrolyte at high voltage,[11] leading to enhanced rate performance and long cycle life. Benefiting from these strategies, the core–shell PBA could deliver 104.3 mAh g^{-1} at 15 mA g^{-1}. Remarkably, it showed outstanding rate performance with 93.3% and 75.8% capacity retention at 300 and 1500 mA g^{-1}, respectively, as well as impressive cycle performance with nearly 90% specific capacity retained after 1000 cycles and nearly 100% Coulombic efficiency.

Results and Discussion

In X-ray diffraction (XRD) of Ni-HCF, CoNi-HCF, and CoNi-HCF@Ni-HCF (see the Supporting Information, Figure S1), the high crystallinity and Na-rich property of CoNi-HCF@Ni-HCF are indicated by sharp and robust peaks, which result from the low-speed crystallization. Compared with the standard diffraction pattern of PBAs, CoNi-HCF@Ni-HCF demonstrates a monoclinic rather than a typical face-centered cubic structure. The (220), (420), (440), and (620) peaks are split into two near-identical peaks. Similar phase-transition phenomena were reported by previously and result from the high concentration of Na^+ and suppressed defects in the crystal framework through the controlled low-speed crystal growth process.[12] In the Raman spectrum for Ni-HCF, there are two distinctive peaks at 2103.7 and 2136.3 cm^{-1}, whereas that for CoNi-HCF displays three peaks at 2103.7, 2141.9 and 2180.0 cm^{-1}, respectively (Figure S2). The core–shell CoNi-HCF@Ni-HCF gives rise to three Raman peaks at 2107.2, 2144.1, and 2182.2 cm^{-1}, which lie between the core (CoNi-HCF) and shell (Ni-HCF) spectra, indicating that the surface of the core material is successfully coated by shell material. In the infrared spectra (Figure S3), the sharp absorptions at 1621 and 3550 cm^{-1} are related to O–H stretching and H–O–H bending, which are caused by the interstitial and absorbing water, the peaks around 2090 cm^{-1} are caused by the CN^- bonding with $Fe^{2+/3+}$. In thermogravimetric analysis (Figure S4), the mass retention before 300 °C of the core and the shell are 86.06% and 85.28%, respectively. The weight loss could be due to the adsorbed and coordinated water, whereas the water content in the crystal framework remains stable after the coating process.

Scanning electron microscopy (SEM) patterns show that both CoNi-HCF and CoNi-HCF@Ni-HCF nanocubes are monodisperse with uniform sizes of 100 and 130 nm, respectively (Figure 2). After coating, the core–shell CoNi-HCF@Ni-HCF retains the cubic morphology, which is probably due to the aforementioned low-speed coprecipitation synthesis method. Transmission electron microscopy (TEM) figures further identify that Ni-HCF is uniformly coated on the surface of CoNi-HCF and forms a smooth shell with a thickness of 15 nm. According to the

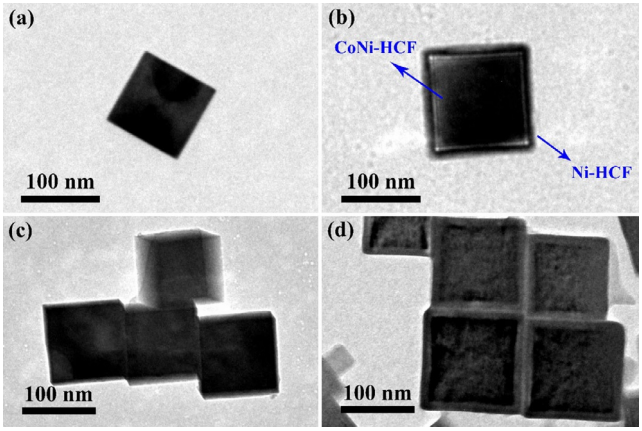


Figure 2. Morphology characterization of CoNi-HCF and core–shell CoNi-HCF@Ni-HCF: a, b) SEM images of CoNi-HCF and CoNi-HCF@Ni-HCF. c, d) TEM images of CoNi-HCF and CoNi-HCF@Ni-HCF.

weight before and after the coating process, the mass ratio of core to shell is around 10:7 and could be optimized by modifying the ratio of raw materials and, in addition, by increasing the ratio of chelating agent, the particle size distribution would be increased simultaneously.

To investigate the practical application of core–shell PBAs as cathode materials for SIBs, the electrochemical performance was studied at an ultrahigh mass loading (6 mg cm^{-2}). Figure 3a and b show the charge–discharge curves of CoNi-HCF and CoNi-HCF@Ni-HCF at 15 mA g^{-1}. Owing to the reversible Na^+ storage offered by coating material Ni-HCF, the specific capacity only reduces slightly from 129.2 to 104.3 mAh g^{-1} after coating and Coulombic Efficiency are 96.1% and 96.3% before and after coating, respectively, corresponding to 1.52 and 1.23 Na^+ reversible storage per formula. Cyclic voltammetry (CV) of CoNi-HCF@Ni-HCF electrode carried out at 0.1 mV s^{-1} from 2.0 to 4.2 V (Figure 3) gave rise to two well-defined symmetric redox peaks at 3.56 and 3.10 V, corresponding to the redox of Fe^{2+} and Fe^{3+}. The CV curves in the following cycles overlap well, showing the highly reversible redox reaction of the active materials. The peaks at 3.86 and 3.73 V for CoNi-HCF can be ascribed to the redox reaction of Co^{2+} and Co^{3+} binding to N. Remarkably, the oxidation peaks at 4.15 V almost disappeared in the core–shell PBA, demonstrating that the shell materials effectively avoid the side reaction between the core material and the electrolyte at the voltages higher than 4.0 V.

© 2019 Wiley-VCH Verlag GmbH & Co. KGaA, Weinheim

1864564x, 2019, 21, Downloaded from https://chemistry-europe.onlinelibrary.wiley.com/doi/10.1002/cssc.201902013 by City University Of Hong Kong, Wiley Online Library on [23/08/2025]. See the Terms and Conditions (https://onlinelibrary.wiley.com/terms-and-conditions) on Wiley Online Library for rules of use; OA articles are governed by the applicable Creative Commons License

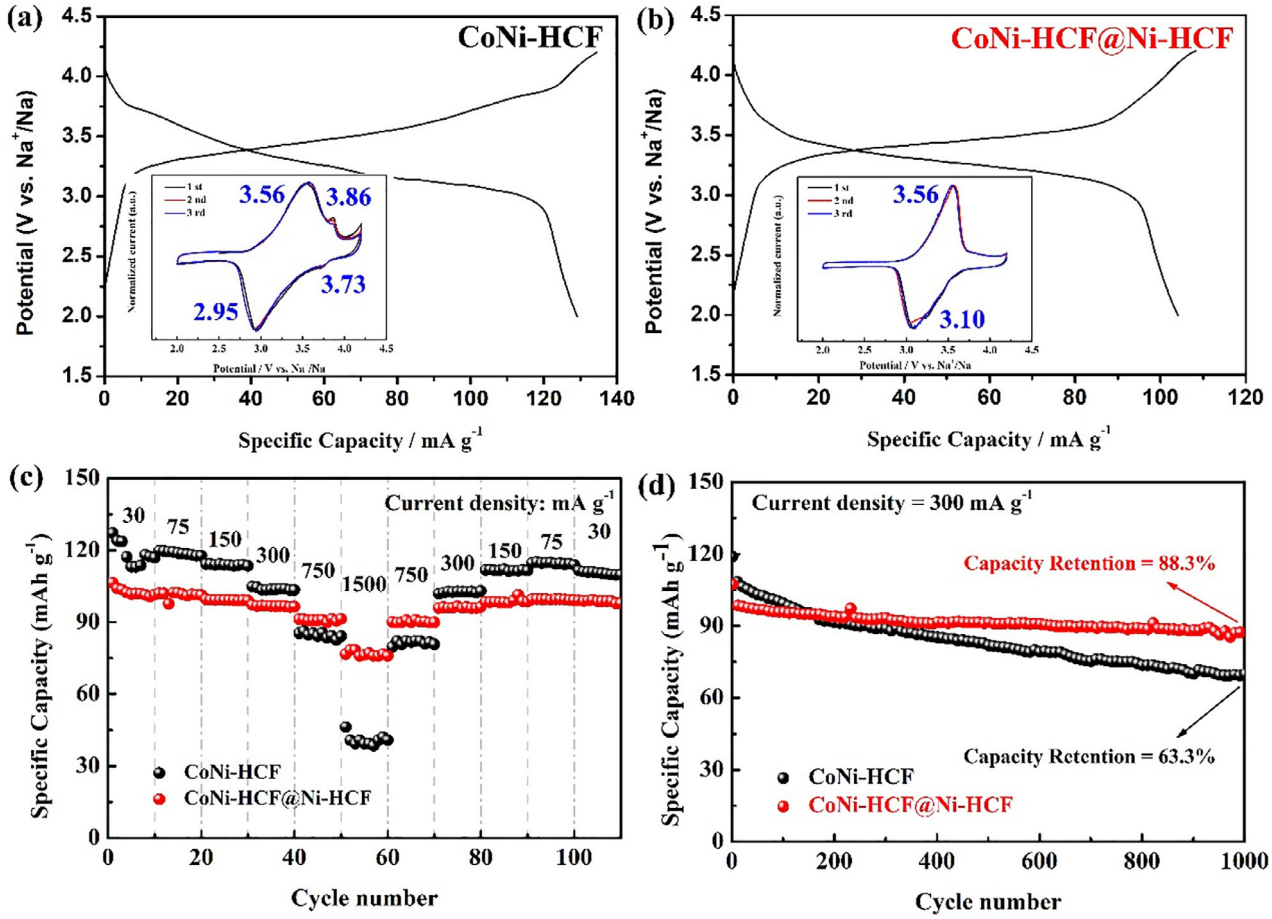


Figure 3. Electrochemical performance: a,b) Charge–discharge voltage profiles at a current density of 15 mA g^{-1} and typical CV curves measured at a scan rate of 0.1 mV s^{-1} for CoNi-HCF (a) and CoNi-HCF@Ni-HCF (b). c) Rate performance at current densities from 30 to 1500 mA g^{-1}. d) Long-term cycling performance at a current density of 300 mA g^{-1}.

Figure 3c shows the rate performances of CoNi-HCF and CoNi-HCF@Ni-HCF at 30–1500 mA g^{-1}. Owing to the shell materials' capacity retention of around 77% at 4250 mA g^{-1}[5b,12d] and lower activation energy, as expected, the core–shell-structured CoNi-HCF@Ni-HCF exhibits an enhanced rate performance, especially at high current density. The discharge capacity remained 79.1 mAh g^{-1} at 10C (1C = 150 mA g^{-1}), owing to the capacity of the shell materials, whereas that of CoNi-HCF was only 40.7 mAh g^{-1} at 10C. CoNi-HCF@Ni-HCF shows superior rate performance at higher current densities (98.7, 96.5, 90.6 and 79.1 mAh g^{-1} at 1, 2, 5 and 10C, respectively). Its capacity recovers to its initial value on returning to 1C.

The long-term cycling performance of CoNi-HCF@Ni-HCF was investigated at 2C and exhibited an improved cycling life compared with CoNi-HCF (Figure 3d). CoNi-HCF@Ni-HCF exhibits a capacity of 98.7 mAh g^{-1} at the 6th cycle after 5 activating cycles under 0.1C, with a capacity retention of 88.3% over 1000 cycles. The capacity decay rate of CoNi-HCF@Ni-HCF is 0.0117% per cycle, which is much lower than that of 0.0367% for CoNi-HCF. Because of the structural stability during the Na^+ insertion and extraction and chemical stability of Ni-HCF in the electrolyte, which could remain at nearly 100% of its initial capacity, even over 1000 cycles, the cyclability of CoNi-HCF is remarkably improved after being coated by Ni-HCF with coulombic efficiency of around 100%. Thus, by integrating the advantages of both the core and shell materials, the multimetal core–shell CoNi-HCF@Ni-HCF shows excellent cycling performance. Moreover, as shown by SEM and TEM (Figure S5), the morphology of the core–shell materials remains stable after cycling.

According to ex situ XRD (Figure 4), when the potential of CoNi-HCF@Ni-HCF reaches 2.0 V, the diffraction peak around 24.5° splits into two with equal intensities, corresponding to a monoclinic structure, owing to the large amount of Na^+ in the framework. When the CoNi-HCF@Ni-HCF electrode is charged from 2.0 V to 3.4 V with an ongoing extraction of Na^+, the gap between the two peaks at 24.5° became smaller, corresponding to the monoclinic structure. From 3.4 V to 4.2 V, the doublet merged into a single sharp peak at around 24.5°, manifesting the phase transition of CoNi-HCF@Ni-HCF from a monoclinic structure to a cubic one. This process is a result of Na^+ extraction from the framework. In the discharging process, the peak near 24.5° reverts to two peaks from a single one and restores the initial state, indicating a reversible phase transition between cubic and monoclinic phases. The peak at around 17° slightly shifts from 17.02 to 17.34° in the overall charging pro-

© 2019 Wiley-VCH Verlag GmbH & Co. KGaA, Weinheim

1864564x, 2019, 21, Downloaded from https://chemistry-europe.onlinelibrary.wiley.com/doi/10.1002/cssc.201902013 by City University Of Hong Kong, Wiley Online Library on [23/08/2025]. See the Terms and Conditions (https://onlinelibrary.wiley.com/terms-and-conditions) on Wiley Online Library for rules of use; OA articles are governed by the applicable Creative Commons License

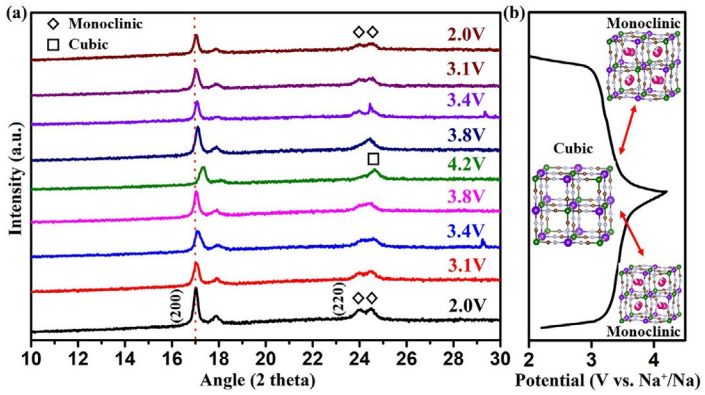


Figure 4. Ex situ XRD: a) XRD patterns at different states. b) The corresponding charge–discharge process of the CoNi-HCF@Ni-HCF at a current density of 15 mA g^{-1} and illustration of the phase transition.

cess, suggesting a negligible lattice parameter change during the cycling process. This zero-strain behavior is also shown by $Li_4Ti_5O_{12}$, a well-known electrode material for LIBs.[13] The negligible volume distortion during cycling is because of the stability of the crystal structure and protection of "zero-strain" Ni-HCF shell, leading to the improved cycling performance and Coulombic efficiency. The entire redox mechanism can be expressed by Equations (1)–(3) ($0 \le x \le 1$):[5b,12d]

Step 1 :

$$\text{Monoclinic } Na_2Ni^{II}Fe^{II}(CN)_6 \leftrightarrow \text{Cubic } NaNi_x^{II}Fe^{III}(CN)_6 + Na^+ + e^- \quad (1)$$

Step 2 :

$$\text{Monoclinic } Na_2Co_{1-x}^{II}Ni_x^{II}Fe^{II}(CN)_6 \leftrightarrow \text{Cubic } NaCo_{1-x}^{II}Ni_x^{II}Fe^{III}(CN)_6 + Na^+ + e^- \quad (2)$$

Step 3 :

$$\text{Cubic } NaCo_{1-x}^{II}Ni_x^{II}Fe^{III}(CN)_6 \leftrightarrow \text{Tetragonal } Na_0Co_{1-x}^{III}Ni_x^{II}Fe^{III}(CN)_6 + Na^+ + e^- \quad (3)$$

To study the cycling mechanism of the core–shell-structured PBA, we prepared a home-made half-cell to monitor the ion concentration in the electrolyte by inductively coupled plasma optical emission spectroscopy (ICP-OES). As shown in Table S1, the $Fe^{2+/3+}$ concentration of the samples is CoNi-HCF > CoNi-HCF@Ni-HCF > Ni-HCF after 500 charge-discharge cycles at 2 C. As a result, we could conclude that the $Fe(CN)_4^{2-}$ anions are more likely to be broken under long cycling and dissolved into the electrolyte, resulting in capacity fading (Figure 5). Therefore, the stability of cobalt-based PBAs could be remarkably enhanced through a dual-level controlling charge–discharge depth mechanism: firstly, the core materials with tunable Ni/Co ratio, few vacancies, and low crystal water content undergoes minor lattice variation during cycling, leading to a better cycling and rate performance. Secondly, the shell materials could significantly reduce the side reaction between the core materials and the $NaClO_4$ in carbonic ester-based electrolyte above 4.0 V and suppress the loss redox-active $Fe(CN)_4^{2-}$ octahedra from the PBAs.

Conclusion

We developed a facile in situ self-assembly method to prepare low-defect core–shell PBAs. The key advantages of this core–shell structure are the suppression of lattice distortion and avoidance of side reactions during the insertion and extraction process. Benefiting from the specially designed structure, the CoNi-HCF@Ni-HCF PBA showed superior rate and cycling performance through a dual-level controlling charge–discharge depth mechanism. Meanwhile, CoNi-HCF@Ni-HCF showed a high specific capacity of 104.3 mAh g^{-1}, a superior rate performance of 79.1 mAh g^{-1} at 10 C, and a long cycling lifespan of over 1000 cycles. The results indicate that this is a practical method for energy storage by rechargeable batteries based on

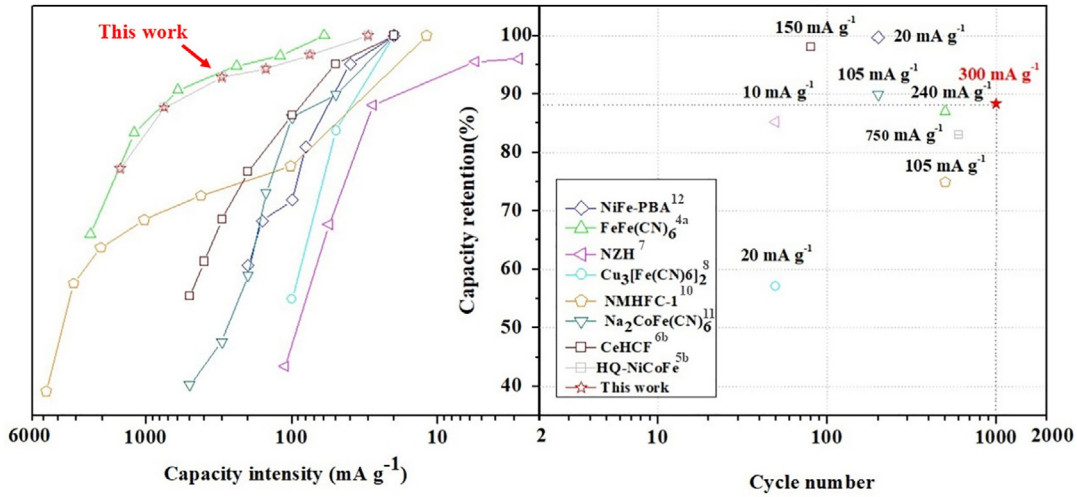


Figure 5. Rate performance and capacity retention of CoNi-HCF@Ni-HCF compared to previously reported PBA cathode materials.

© 2019 Wiley-VCH Verlag GmbH & Co. KGaA, Weinheim

1864564x, 2019, 21, Downloaded from https://chemistry-europe.onlinelibrary.wiley.com/doi/10.1002/cssc.201902013 by City University Of Hong Kong, Wiley Online Library on [23/08/2025]. See the Terms and Conditions (https://onlinelibrary.wiley.com/terms-and-conditions) on Wiley Online Library for rules of use; OA articles are governed by the applicable Creative Commons License

1864564x, 2019, 21, Downloaded from https://chemistry-europe.onlinelibrary.wiley.com/doi/10.1002/cssc.201902013 by City University Of Hong Kong, Wiley Online Library on [23/08/2025]. See the Terms and Conditions (https://onlinelibrary.wiley.com/terms-and-conditions) on Wiley Online Library for rules of use; OA articles are governed by the applicable Creative Commons License

core–shell MOFs and also that core–shell PBAs could serve as cathodes for novel batteries.

Experimental Section

Preparation of CoNi-HCF.

All chemicals were purchased from Aladdin and used without further purifications. We prepared CoNi-HCF by the following steps: $CoCl_2$ (3.5 mmol), $NiCl_2$ (1.5 mmol), and sodium citrate (5 mmol) were dissolved in DI water (50 mL) to give solution A. $Na_4Fe(CN)_6$ (5 mmol) was dissolved in DI water (50 mL) to give solution B. Polyvinylpyrrolidone (PVP; 2 g) was dissolved in DI water (100 mL) to give solution C. Solutions A and B were slowly added into solution C. After continuous stirring for 6 h and aging for 24 h at room temperature, the precipitate was collected by centrifugation at 5000 rpm and washed three times with DI water and ethanol (400 mL). Finally, the precipitate was dried at 100 °C in a vacuum oven for 24 h.

Synthesis of CoNi-HCF@Ni-HCF.

To prepare CoNi-HCF@Ni-HCF, $CoCl_2$ (3.5 mmol), $NiCl_2$ (1.5 mmol), and sodium citrate (5 mmol) were dissolved in DI water (50 mL) to give solution A. $Na_4Fe(CN)_6$ (5 mmol) was dissolved in DI water (50 mL) to give solution B. Polyvinylpyrrolidone (PVP; 2 g) was dissolved in DI water (100 mL) to give solution C. Solutions A and B were slowly added into solution C under continuous stirring for 6 h to form solution D. After aging for 24 h at room temperature, solution D was ultrasonically stirred for 20 min. Solution E was prepared by dissolving $NiCl_2{\cdot}6H_2O$ (0.858 g) and sodium citrate (1.98 g) in DI water (60 mL) for coating. Then, $Na_4Fe(CN)_6\times10H_2O$ (1.165 g) and solution E were slowly added into solution D under continuous stirring for 24 h at room temperature. The precipitate was collected by centrifugation and washed three times with DI water and ethanol (400 mL). Finally, the precipitate was dried at 100 °C in a vacuum oven for 24 h.

Electrochemical measurements

To evaluate the electrochemical performance of CoNi-HCF and CoNi-HCF@Ni-HCF, working electrodes were made by reeling a mixture of 70 wt% Co-Ni-HCF or CoNi-HCF@Ni-HCF, 20 wt% Ketjen black, and 10 wt% polytetrafluoroethylene (PTFE) into a thin film pressed onto aluminum mesh. The electrochemical performance was measured with standard CR2032 coin cells by using metallic sodium as counter electrode and porous glass fibers (GF/A) from Whatman as separator. The electrolyte was 1.0 mol L^{-1} $NaClO_4$, with ethylene carbonate/diethyl carbonate (1:1 *v/v*) solution with 2 wt% fluoroethylene carbonate as solvent. Each cell was assembled in an Ar-filled glove box and tested at ambient temperature. Cyclic voltammetry (CV) was carried out on a Princeton electrochemical workstation from 2.0 to 4.2 V at a scan rate of 0.1 mV s^{-1}. The galvanostatic charge–discharge tests were performed on a Wuhan LAND-CT2001A battery testing system from 2.0 to 4.2 V.

Acknowledgements

The authors thank the National Key R&D Program of China (Grant Nos. 2016YFB0700600 and 2016YFB010030X) and National Natural Science Foundation of China (Grant Nos. 51732005 and 51772117) for funding this work. We also acknowledge the measurements provided by the Analytical and Testing Centre and the State Key Laboratory of Materials Processing and Die & Mould Technology of HUST.

Conflict of interest

The authors declare no conflict of interest.

Keywords: batteries · core–shell structures · electrodes · metal–organic frameworks · self-assembly

[1] a) M. Armand, J.-M. Tarascon, *Nature* **2008**, *451*, 652; b) H. Liu, F. C. Strobridge, O. J. Borkiewicz, K. M. Wiaderek, K. W. Chapman, P. J. Chupas, C. P. Grey, *Science* **2014**, *344*, 1252817; c) M. R. Palacín, A. de Guibert, *Science* **2016**, *351*, 1253292; d) B. Wang, Y. Han, X. Wang, N. Bahlawane, H. Pan, M. Yan, Y. Jiang, *iScience* **2018**, *3*, 110.

[2] a) C. D. Wessells, S. V. Peddada, R. A. Huggins, Y. Cui, *Nano Lett.* **2011**, *11*, 5421; b) Z. Li, K. Xiang, W. Xing, W. C. Carter, Y. M. Chiang, *Adv. Energy Mater.* **2015**, *5*, 1401410; c) Y. Liu, Y. Qiao, W. Zhang, Z. Li, X. Ji, L. Miao, L. Yuan, X. Hu, Y. Huang, *Nano Energy* **2015**, *12*, 386.

[3] a) M. Pasta, C. D. Wessells, R. A. Huggins, Y. Cui, *Nat. Commun.* **2012**, *3*, 1149; b) H. Pan, Y.-S. Hu, L. Chen, *Energy Environ. Sci.* **2013**, *6*, 2338; c) P. Barpanda, G. Oyama, S.-I. Nishimura, S.-C. Chung, A. Yamada, *Nat. Commun.* **2014**, *5*, 4358; d) C. Fang, Y. Huang, W. Zhang, J. Han, Z. Deng, Y. Cao, H. Yang, *Adv. Energy Mater.* **2016**, *6*, 1501727.

[4] a) X. Wu, W. Deng, J. Qian, Y. Cao, X. Ai, H. Yang, *J. Mater. Chem. A* **2013**, *1*, 10130; b) Y. Lu, L. Wang, J. Cheng, J. B. Goodenough, *Chem. Commun.* **2012**, *48*, 6544; c) Y. You, X.-L. Wu, Y.-X. Yin, Y.-G. Guo, *Energy Environ. Sci.* **2014**, *7*, 1643; d) L. Wang, J. Song, R. Qiao, L. A. Wray, M. A. Hossain, Y.-D. Chuang, W. Yang, Y. Lu, D. Evans, J.-J. Lee, *J. Am. Chem. Soc.* **2015**, *137*, 2548; e) X. Wu, J. J. Hong, W. Shin, L. Ma, T. Liu, X. Bi, Y. Yuan, Y. Qi, T. W. Surta, W. Huang, *Nat. Energy* **2019**, *4*, 123; f) H. Lee, Y.-I. Kim, J.-K. Park, J. W. Choi, *Chem. Commun.* **2012**, *48*, 8416; g) S. Jiao, J. Tuo, H. Xie, Z. Cai, S. Wang, J. Zhu, *Mater. Res. Bull.* **2017**, *86*, 194.

[5] a) X. Wu, Y. Luo, M. Sun, J. Qian, Y. Cao, X. Ai, H. Yang, *Nano Energy* **2015**, *13*, 117; b) J. Peng, J. Wang, H. Yi, W. Hu, Y. Yu, J. Yin, Y. Shen, Y. Liu, J. Luo, Y. Xu, *Adv. Energy Mater.* **2018**, *8*, 1702856.

[6] a) X. Wu, Y. Qi, J. J. Hong, Z. Li, A. S. Hernandez, X. Ji, *Angew. Chem. Int. Ed.* **2017**, *56*, 13026; *Angew. Chem.* **2017**, *129*, 13206; b) J. Peng, C. Li, J. Yin, J. Wang, Y. Yu, Y. Shen, J. Fang, A. Chen, Y. Xu, R. Rehman, *ACS Appl. Energy Mater.* **2019**, *2*, 187; c) J. Qian, C. Wu, Y. Cao, Z. Ma, Y. Huang, X. Ai, H. Yang, *Adv. Energy Mater.* **2018**, *8*, 1702619.

[7] H.-W. Lee, R. Y. Wang, M. Pasta, S. W. Lee, N. Liu, Y. Cui, *Nat. Commun.* **2014**, *5*, 5280.

[8] Z. Shadike, D.-R. Shi, T.-W. Tian-Wang, M.-H. Cao, S.-F. Yang, J. Chen, Z.-W. Fu, *J. Mater. Chem. A* **2017**, *5*, 6393.

[9] X. Wu, C. Wu, C. Wei, L. Hu, J. Qian, Y. Cao, X. Ai, J. Wang, H. Yang, *ACS Appl. Mater. Interfaces* **2016**, *8*, 5393.

[10] J. Song, L. Wang, Y. Lu, J. Liu, B. Guo, P. Xiao, J.-J. Lee, X.-Q. Yang, G. Henkelman, J. B. Goodenough, *J. Am. Chem. Soc.* **2015**, *137*, 2658.

[11] M. Wan, Y. Tang, L. Wang, X. Xiang, X. Li, K. Chen, L. Xue, W. Zhang, Y. Huang, *J. Power Sources* **2016**, *329*, 290.

[12] a) X. Wu, M. Sun, S. Guo, J. Qian, Y. Liu, Y. Cao, X. Ai, H. Yang, *ChemNanoMat* **2015**, *1*, 188; b) Y. You, H. R. Yao, S. Xin, Y. X. Yin, T. T. Zuo, C. P. Yang, Y. G. Guo, Y. Cui, L. J. Wan, J. B. Goodenough, *Adv. Mater.* **2016**, *28*, 7243; c) Y. Huang, M. Xie, J. Zhang, Z. Wang, Y. Jiang, G. Xiao, S. Li, L. Li, F. Wu, R. Chen, *Nano Energy* **2017**, *39*, 273; d) Y. Xu, J. Wan, L. Huang, M. Ou, C. Fan, P. Wei, J. Peng, Y. Liu, Y. Qiu, X. Sun, *Adv. Energy Mater.* **2019**, *9*, 1803158.

[13] Y. You, X.-L. Wu, Y.-X. Yin, Y.-G. Guo, *J. Mater. Chem. A* **2013**, *1*, 14061.

Manuscript received: July 23, 2019
Revised manuscript received: August 22, 2019
Accepted manuscript online: August 25, 2019
Version of record online: October 10, 2019

© 2019 Wiley-VCH Verlag GmbH & Co. KGaA, Weinheim